SOFT ROBOTS

Hygrobot: A self-locomotive ratcheted actuator powered by environmental humidity

Beomjune Shin,[1] Jonghyun Ha,[1] Minhee Lee,[1] Keunhwan Park,[1] Gee Ho Park,[2] Tae Hyun Choi,[3] Kyu-Jin Cho,[1,4] Ho-Young Kim[1,4]*

Microrobots that are light and agile yet require no artificial power input can be widely used in medical, military, and industrial applications. As an actuation system to drive such robots, here we report a biologically inspired bilayer structure that harnesses the environmental humidity energy, with ratchets to rectify the motion. We named this actuator-ratchet system the hygrobot. The actuator uses a hygroscopically responsive film consisting of aligned nanofibers produced by directional electrospinning, which quickly swells and shrinks in lengthwise direction in response to the change of humidity. The ratchets based on asymmetric friction coefficients rectify oscillatory bending motion in a directional locomotion. We mathematically analyzed the mechanical response of the hygrobot, which allowed not only prediction of its performance but also the optimal design to maximize the locomotion speed given geometric and environmental constraints. The hygrobot sterilized a trail across an agar plate without any artificial energy supply.

INTRODUCTION

Microrobots can perform various functions by interacting with the surroundings for medical, military, industrial, or environmental purposes. One of the major challenges faced by microrobotic engineering is a lack of power sources to drive robots without needing artificial intervention. Among many attempts to address this issue, we pay special attention to plants because they generate motions and deformations with a very simple structure, unlike animals relying on the complex of motor proteins, or muscles. Most botanical movements are hydraulic in nature; that is, simple transport of fluid (mostly water) in and out of the plant tissue generates motions. In particular, hygroexpansive properties of plant cells, leading to volumetric change in response to moisture content, are exploited by many plants, as seen in opening and closing of pine cones (*1*); self-digging of seeds of wild wheat (*2*), *Erodium* (*3*), and *Pelargonium* (*4*); self-sealing of pollen grains (*5*); and opening of seed pods (*6*) and ice plant capsules (*7*).

Various soft materials are responsive to external stimuli—such as heat (*8*, *9*), light (*10*–*12*), and chemical substances (*13*–*17*)—and interest in actuators using hygroexpansive materials either artificial or natural is growing recently thanks to the potential to harness energy from environmental humidity change. Paper is probably the most easily accessible example of such actuators, which bends due to strain gradient in thickness-wise direction when placed near a wet substrate (*18*–*20*). Artificially synthesized polymers (*21*) and biological materials like *Bacillus* spores (*22*) have been used to achieve similar hygroscopic actuation, which can be used for electrical power generation and locomotion.

However, there are challenges with implementing hygroscopic actuation mechanisms to power microrobots. First, the response of the overall actuation system should be agile enough for practical use. A thin hygroscopic layer can hasten the response but may result in the sacrifice of actuation magnitude. Second, the actuation should be possible without artificial control of atmospheric humidity condition. Many previously demonstrated hygroscopic actuators move when humidity is raised either by external supply of water vapor or by placement near a water source. For repeated motion, humidity levels should be periodically decreased as well, which has required human intervention or complicated and bulky mechanical mechanisms (*23*). Third, the movement should be regulated to achieve locomotion in a desired direction. Thin sheets of paper (*20*) and polymers (*21*) were shown to flip repeatedly on a moist surface owing to natural drying of a part far from a vapor source, but their tumbling hardly gives any directional locomotion. Fourth, a mathematical understanding of the dynamic response of the hygroscopic actuation has been rarely attempted, which should play a pivotal role in obtaining the optimal design.

To meet the foregoing challenges, here we report a hygroscopically powered robot, named hygrobot, that locomotes spontaneously in a ratcheted fashion on a moist surface at a speed high enough to enable practical applications. Also, we mathematically analyzed the motion of the hygrobot, which allows us to obtain optimal geometric design to maximize the locomotion speed. The mathematical model couples the moisture diffusion and elastic bending of the actuator plate. We used an inexpensive, commercially available hygroscopic material instead of specially prepared polymers or biomaterials that are not easily accessible to most robotic engineers. A manufacturing process is described to increase the actuation speed and strain of the material in response to humidity change. A simple mechanism is attached to the actuator to enable autonomous yet directional locomotion. Last, we demonstrate a possible application of the hygrobot for biomedical treatments on a wet skin.

RESULTS

Hygroscopic response of the bending actuator

Tissues of many motile plants, such as pine cone (*1*), awns of wild wheat (*2*), and *Erodium* (*24*), use a bilayer structure, one layer of which is hygroscopically active, whereas the other layer is hygroscopically inactive. Although such bilayer configuration has been mimicked frequently (*10*, *18*, *21*, *22*), aligned microstructures of the plant tissues have drawn relatively little attention, despite their critical role in effective

[1]Department of Mechanical and Aerospace Engineering, Seoul National University, Seoul 08826, Korea. [2]Interdisciplinary Program in Stem Cell Biology, College of Medicine, Seoul National University, Seoul 03080, Korea. [3]Department of Plastic and Reconstructive Surgery, Institute of Human-Environment Interface Biology, College of Medicine, Seoul National University, Seoul 03080, Korea. [4]Institute of Advanced Machines and Design, Seoul National University, Seoul 08826, Korea.
*Corresponding author. Email: hyk@snu.ac.kr

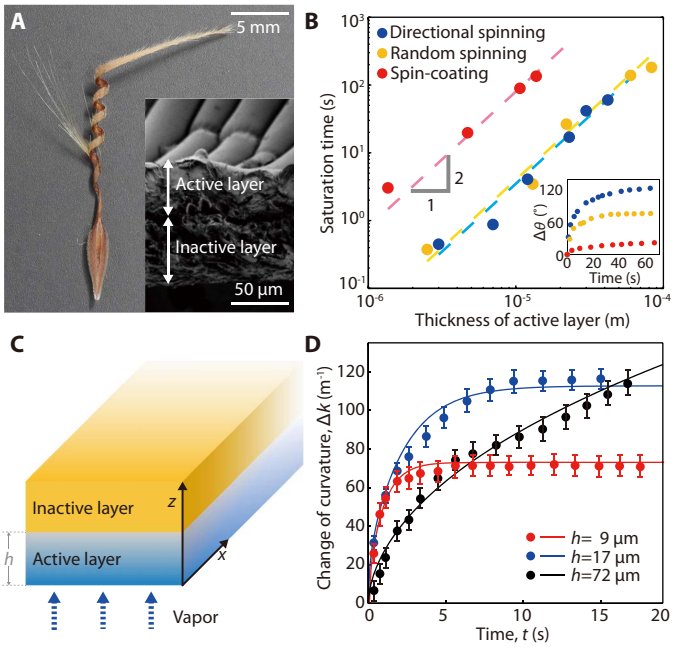

Fig. 1. Hygroscopically responsive bilayer structures. (**A**) Optical image of a seed of *P. carnosum* and the SEM image of the cross-section of its awn. (**B**) Time for saturation of deflection angle versus thickness of active layers fabricated via spin-coating (red circles), random electrospinning (yellow circles), and directional electrospinning (blue circles). The thickness of the inactive layer is 55 μm for all the cases. The trend lines for all the types of active layer follow $t_s \sim h^2$, implying the diffusive transport of moisture in the layers. Inset: Temporal evolution of the deflection angle at the free end of the bilayers, 25 mm in length, whose active layers are fabricated by spin-coating (red circles), random electrospinning (yellow circles), and directional electrospinning (blue circles). The active layer thickness is 35 μm. (**C**) Coordinate system for the bilayer. (**D**) Temporal evolution of the bilayer curvature when the environmental humidity abruptly increases to 0.8 from 0.2 at $t = 0$. Circles and lines correspond to experiment and theory, respectively. Error bars represent SD.

generation of movements. Figure 1A shows the cross-section of an awn of *Pelargonium carnosum* seed, consisting of hygroscopically active cells aligned on a hygroscopically inactive layer. The awn is responsible for the propulsion of the seed into the soil by stretching when wet but helically coiling when dry. The deformation mode of the awn is determined by both the cell alignment direction and the arrangement of cellulose microfibrils winding up the cell walls. Such alignment of hygroresponsive cells—found in *Selaginella lepidophylla* (*25*), awns of Stork's bill (*24*), as well as *Pelargonium* species—inspired us to adopt the structure to facilitate and to magnify deformation of the actuator in a desired direction.

We fabricated an aligned structure of hygroscopic PEO (polyethylene oxide) nanofibers via the directional electrospinning. To test the effectiveness of the nanofiber alignment in hygroscopic actuation, we compared the bending characteristics of the bilayers with aligned PEO fibers, randomly spun PEO fibers, and spin-coated PEO film of the same dimensions. Their length and inactive layer thickness are 25 mm and 55 μm, respectively. We abruptly raised the relative humidity of the air surrounding the actuators from 20 to 80% at 25°C within a closed chamber; the actuator bent toward the inactive layer due to hygroscopic expansion of the active layer.

The deflection angle at the free end versus time is plotted in the inset of Fig. 1B. Defining the time when the deflection angle reaches 90% of its maximum value as the saturation time, t_s, we plotted t_s of the hygroscopic actuators versus the thickness of the active layer, h (Fig. 1B). The response time of the electrospun layers is only 20% of the spin-coated structure. In addition to the fast response of the electrospun aligned structure, its maximum deflection angle is 5.6 and 1.7 times greater than those of the spin-coated and the randomly electrospun actuators, respectively. Furthermore, the bending of the aligned structure occurs in a single direction due to the uniform longitudinal swelling of fiber arrays, unlike the spin-coated and randomly electrospun ones that bend and twist in a random fashion. The irregular directions of bending and twisting of previous hygroscopic actuators make it nearly impossible to control their wriggling trajectory, severely limiting their use as a robotic actuator (*20*, *21*).

In Fig. 1B, t_s increases with h^2, implying that the hygroexpansion occurs as water molecules diffuse into the active layer (*26*). The plot also allows us to obtain the effective diffusivity, D, defined as $D = h^2/t_s$, of the water molecules in the active layers: 0.9×10^{-10} m^2/s for the electrospun fiber layers and 1.2×10^{-12} m^2/s for the spin-coated layers.

We attribute the orders-of-magnitude improvement of the diffusivity in the aligned fiber structure primarily to its high porosity. The pores between nanofibers provide gaseous paths of water molecules instead of a solid barrier as experienced in the spin-coated layer. The effective diffusivity, D_e, for a binary medium can be estimated by the following relation (*27*): $(D_e - D_s)/(D_e + 2D_s) \sim \eta(D_a - D_s)/(D_a + 2D_s)$, where η is the porosity of the electrospun layer, and D_a and D_s are the water vapor diffusivity in the air and the solid polymer, respectively. Substituting $\eta = 0.7$ as obtained by comparing the densities of the porous and dense PEO layers, we calculated D_a to be 2.82×10^{-5} m^2/s (*28*). $D_s = 1.2 \times 10^{-12}$ m^2/s as obtained from Fig. 1B, so we write $D_e \sim 1 \times 10^{-11}$ m^2/s, which agrees with the foregoing estimate.

The diffusive transport of moisture in the hygroscopically active layer allows us to compute the transient bending response of the bilayer actuator using the theory of elasticity. The one-dimensional diffusion of the water molecules follows $\partial\phi/\partial t = D\partial^2\phi/\partial z^2$, where $\phi(z, t)$ is the water concentration, t is time, and z designates the thickness direction as shown in Fig. 1C. With the initial concentration $\phi(z, 0) = \phi_0$, the concentration distribution in the active layer ($0 < z < h$), which is subjected to the boundary conditions of $\phi(0, t) = \phi_\infty$ on the outer surface and $\partial\phi(h, t)/\partial z = 0$ on the interface of the active and inactive layers, is given by

$$\phi(z,t) = \sum_{n=0}^{\infty} \frac{-2(\phi_0 - \phi_\infty)}{(n+1/2)\pi} e^{-\lambda_n^2 t} \sin\frac{(n+1/2)\pi z}{h} + \phi_\infty$$

Here, $\lambda_n = D^{1/2}(n + 1/2)\pi/h$, and ϕ_∞ is the environmental humidity.

The local moisture concentration induces the hygroscopic strain $\varepsilon_h = \alpha\phi$, where α is the hygroscopic expansion coefficient, 0.05, as empirically measured for the active layer with aligned nanofibers. The total strain in the active layer is given by $\varepsilon(z, t) = \varepsilon_0 - \kappa\zeta - \varepsilon_h$, where ε_0 is the reference strain at the reference plane, ζ is the distance from the reference plane, and κ is the bending curvature. The local stress, σ, equals $E\varepsilon$, with E being Young's modulus. E of the active layer was measured as a function of ϕ in a constant humidity chamber separately to give $E = -77.4\phi + 169.2$ MPa. The absence of any external loads led us to write the force $F = \int\sigma d\zeta = 0$ and the moment $M = \int\sigma\zeta d\zeta = 0$ throughout the active and inactive layers. The change of curvature of the bilayer from the base (dry) state, obtained by numerical integration of the force and moment, is plotted in Fig. 1D. The initial change

of the bending curvature with the diffusion influx of water molecules and the later saturation of the curvature due to concentration equilibrium with the environments were predicted well by our theory. It not only validated the diffusion-coupled elastic bending model but also indicated that our estimation of diffusivity based on the saturation time in Fig. 1B is reasonable. The time for curvature saturation increased with the thickness of the active layer, whereas the thickness of the inactive layer h_i was fixed at 55 μm. Upon exposing a hygroscopic actuator to 10^4 cycles of relative humidity variation between 0.2 and 0.8 at 25°C, we found the amount of curvature change to decrease by 17% from the initial value.

Locomotion under temporal humidity variation

The temporal variation of the environmental humidity caused the actuator to alternate the bending directions, enabling its use as a simple energy-harvesting device (*21*, *22*). However, here we transformed symmetric oscillations into a directional motion for locomotive applications. Inspired by the creeping, crawling, and slithering animals like worms, snails, and snakes, which rectify their motion by breaking the symmetry of friction (*29*), we attached legs of very simple geometry at the ends of actuator, as schematically shown in Fig. 2A. Without complicated surface texturing of the footpads (*30*), the motion can be rectified by only folding the legs in the middle, providing an advantage of simplifying the microrobot design. In the following, we describe the strategy of motion rectification.

With the hygroscopically inactive layer beneath the active layer, the dry bilayer is initially bent convex downward. In this configuration, the end tip of the foreleg and the knee (the folded part) of the hind leg is in contact with the substrate. The static friction coefficients of the end tip and knee of the legs made of PET (polyethylene terephthalate) with the substrate, filter paper (GB005 Blotting Paper, Whatman), were respectively measured to be about 1 and 0.5 (see section S3). As the environmental humidity increases, the bilayer bends upward with the swelling of the active layer, thereby bringing the legs closer (Fig. 2A). Because of the difference in the static friction coefficient, the knee of the hind leg slides forward while the foreleg is stationary. When the bilayer reaches the upward convex, the foreleg touches its knee on the substrate while the hind leg stands on its tip. Then, we let the bilayer dry, causing it to return to the initial downward convex, spreading the two legs. The foreleg that kneels slides forward while the hind leg is fixed. By repeating the humidity cycle (Fig. 2B) with alternating supply of water-saturated air and dry nitrogen gas, the directional locomotion of the hygrobot was achieved, which resembled that of inchworms (*31*). The corresponding images and movie are shown in Fig. 2C and movie S1.

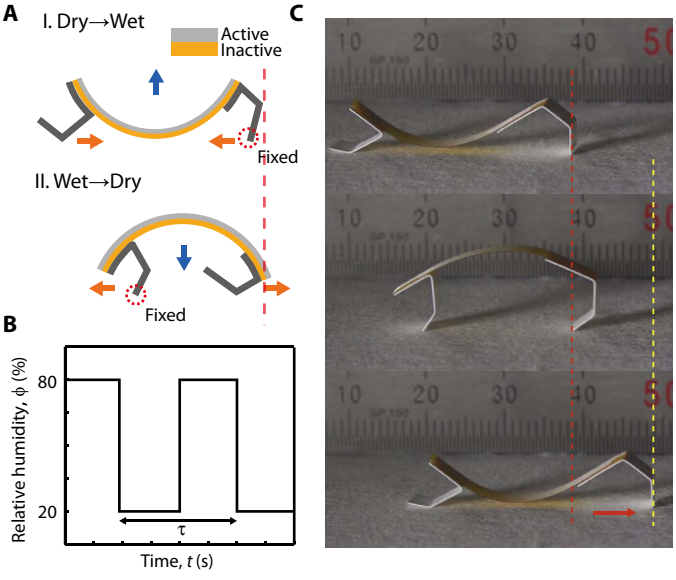

Fig. 2. Ratcheted locomotion of hygrobots. (**A**) Ratcheting of two legs attached to a bilayer actuator. The difference in the static friction coefficients of the end tip and knee of the legs rectifies the motion. (**B**) Artificially controlled temporal variation of the environmental humidity. (**C**) Advance of the hygrobot for a single period of humidity variation. The corresponding movie is shown in movie S1.

Now, we theoretically predict its speed and optimize the design. The distance the hygrobot travels in a period (τ) of humidity cycle is $\Delta l = l - l_p$, where l is the length of the straightened actuator and l_p is the projected length of its arc with the maximum curvature κ_m reached during a period, as illustrated in Fig. 3A. For $l_p = 2\kappa_m^{-1}\sin(l\kappa_m/2)$, one can obtain the locomotion speed $v = \Delta l/\tau$ by calculating κ_m. Our theory to compute $\phi(t, z)$ and subsequently $\kappa(t)$, as delineated above, allows us to find the locomotion speed as a function of various design and environmental parameters, including the bending stiffness of the active and inactive layers, length of the actuator, hygroscopic expansion coefficient of the active layer, and the amplitude and frequency of humidity change.

We plot the theoretical speed v of a hygrobot with h = 13 μm, h_i = 55 μm, and l = 25 mm under the relative humidity oscillation between 0.2 and 0.8 at 25°C as a function of the period τ (Fig. 3B). The decrease in humidity period corresponds to the increase in actuation frequency but shortens the time of moisture diffusion into the active layer. The maximum curvature increased with τ when τ was small. However, the effect of actuation frequency dominated that of the curvature, and thus, v monotonically decreased as τ increased, which agrees well with the experimental results.

Figure 3C plots the dependence of v on h, the thickness of the active layer, when h_i = 55 μm, l = 25 mm, and τ = 2 s under the swing of humidity between 0.2 and 0.8. The velocity v increased with the active layer thickness until h reached about 30 μm, but v decreased afterward. The penetration thickness of moisture through diffusion is scaled as $(D\tau)^{1/2}$ ~ 10 μm. When the active layer was excessively thick, causing only a fraction of the layer to swell, the remaining region only resisted the bending, leading to a decrease of v with h. These experimental results match favorably the theoretical prediction.

We plot v as a function of h and τ with h_i = 55 μm and l = 25 mm (Fig. 3D). Using this contour map, one can find the optimal thickness of the active layer to maximize the locomotion speed when the period of humidity variation is set by the external condition. We compared the performance of the hygrobot with other robots and terrestrial animals on a two-dimensional space constructed with the velocity measured in body length (BL) per second and body mass (Fig. 3E). The robot optimized in Fig. 3C, which has an active layer thickness of 30 μm and a mass of 0.035 g, achieved linear locomotion at a speed of 6 mm/s, or 0.24 BL/s when τ = 2 s. Owing to the hygrobot's superior velocity despite small mass, it is located well above the trend line of the previously reported soft robots, where the locomotion velocity increases with the body mass. The speeds of the terrestrial animals and most of the conventional robots with rigid parts are above 10^0 BL/s regardless of the body mass. The speed of the hygrobot is close to the lower speed limit of the rigid robots. By attaching an additional weight, the hygrobot was found to be able to carry 50 times its weight at half

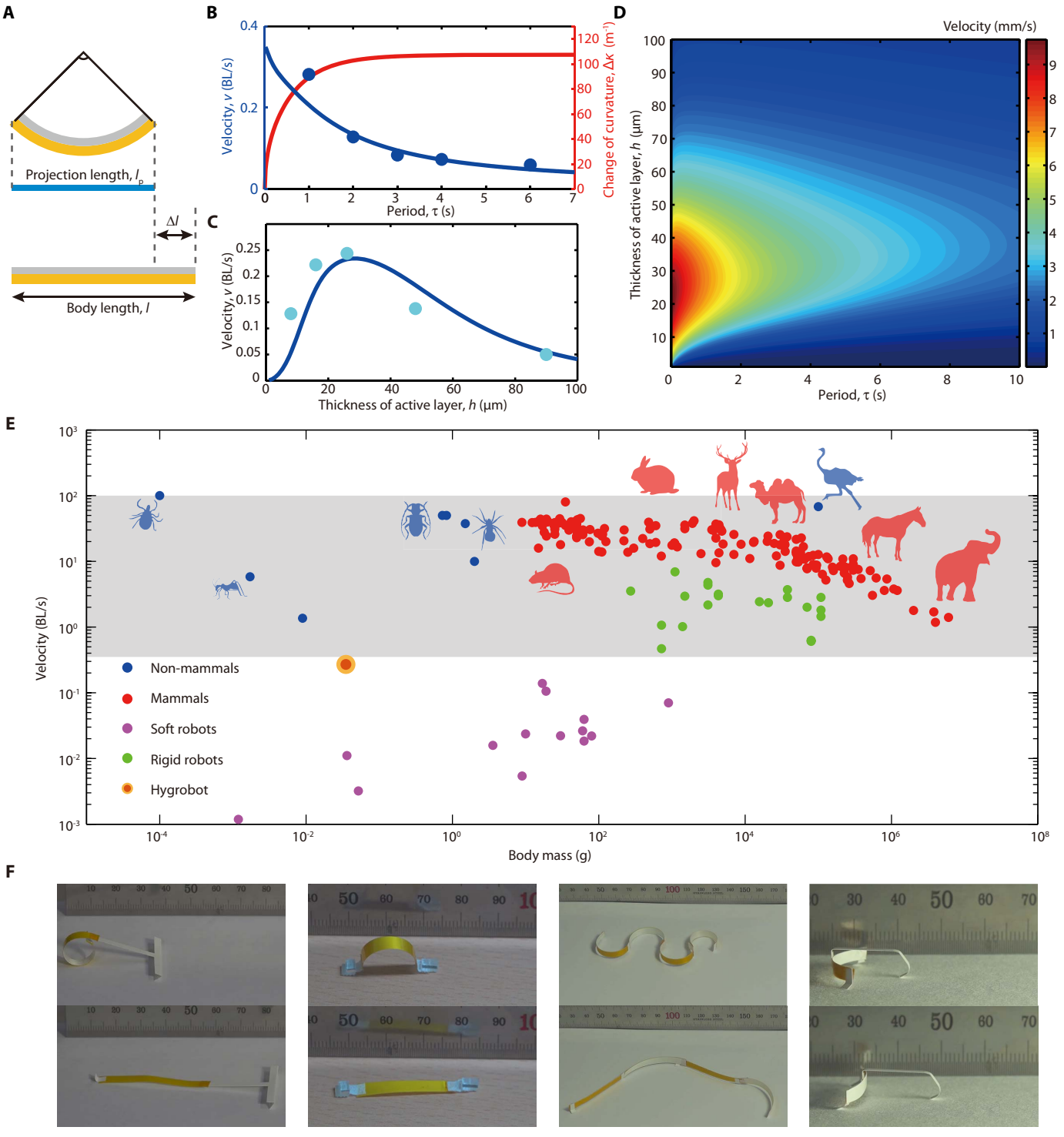

Fig. 3. Velocity of hygrobots. (**A**) The difference between l and l_p corresponds to a distance that a hygrobot advances a period. (**B**) Velocity of hygrobots as a function of the period of humidity variation. Circles correspond to the experimentally measured velocity. Blue and red lines are theoretically calculated velocity and maximum change of curvature, respectively. (**C**) Velocity of hygrobots as a function of the active layer thickness. Circles and lines correspond to experiment and theory, respectively. (**D**) Contour map of the hygrobot velocity as a function of active layer thickness and period. (**E**) Velocity of various animals and robots measured in body length (BL) per second versus body mass. For data, see tables S1 to S3. (**F**) Hygroscopic actuation systems of different designs from Fig. 2C, which can also propel themselves under temporal variation of environmental humidity. The corresponding movie and details are in movie S2 and section S2.

of the speed under free load and to cease to move when the weight increased to 80 times its original value.

A number of different designs in addition to that shown in Fig. 2C can be developed to achieve linear locomotion of the hygroscopic actuator in response to temporal change of environmental humidity. Bending can occur in a plane perpendicular or parallel to the substrate, and ratchets of various types can be devised, as shown in Fig. 3F (details in section S2). Samples of those actuation systems creeping or crawling under varying humidity are shown in movie S2.

Spontaneous locomotion in spatial humidity gradient

Although temporal variation of humidity around the hygrobot can occur naturally via human breathing or day-night humidity cycle (*3*), here we show that it can propel itself spontaneously when placed on a moist surface. Figure 4A displays the experimentally measured humidity distribution of quiescent air near a moist surface using a humidity sensor (Sensirion EK-H5) at 23°C. The relative humidity decreases with distance from a damp filter paper, a significant change occurring within 10 mm. The hygrobot exploits this spatial gradient of humidity by oscillating between the regions of high and low humidity. The shape change is similar to what is shown in Fig. 2A. Being convex toward the hygroscopically active layer when dry, the initially dry bilayer placed on the moist surface turns convex upward (or toward the inactive layer) because the active layer swells due to a high humidity near the substrate. When convex upward, the hygrobot dries by losing moisture to the local environment of low humidity and returns to the downward convex.

Because the motion strategy similar to that under the temporal oscillation of humidity is adopted, we use a similar ratchet system having the asymmetric friction coefficient. However, in this case, the ratchet has been designed to maximize the displacement of the hygrobot in the vertical direction to fully exploit the humidity difference (section S4). When the humidity around the bilayer is high (mode I in Fig. 4B), the legs are pulled together because of bilayer bending, but only the hind leg moves because its friction coefficient is less than that of the foreleg. When the bilayer is dried (mode II in Fig. 4B), the legs are pushed apart as the bilayer is stretched out, causing only the foreleg to move because of its lower friction coefficient than that of the hind leg. The experimental images of the hygrobot that propels itself using the spatial humidity gradient are shown in Fig. 4B. The distance that a hygrobot (where the thickness of the active and inactive layers is 35 and 55 μm, respectively, and the length is 15 mm) travels with time is shown in Fig. 4C.

We estimate the locomotion speed of the hygrobot driven by the spatial gradient of humidity in the following. The theoretical model built for the speed of the hygrobot under temporal variation of humidity can be used once the period (τ) and magnitude (Δϕ) of humidity oscillation are specified. Because the humidity variation is caused by bending of the hygrobot, the time scale of the moisture diffusion into the active layer, which determines the bending time, gives τ. For a cycle of moisture transfer in and out of the active layer, $\tau \sim 2h^2/D \sim 2$ s, which is consistent with the experimental observation. The magnitude of humidity oscillation is determined by the humidity

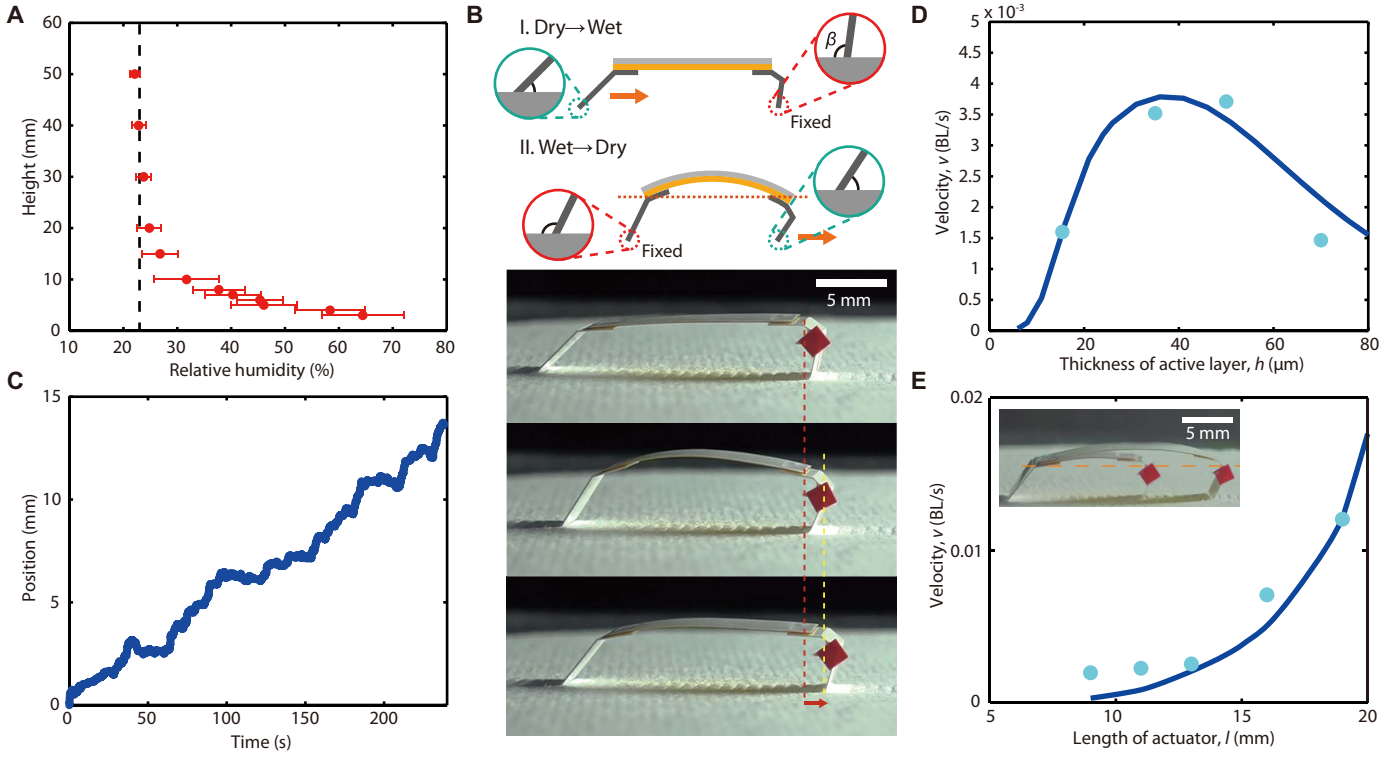

Fig. 4. Spontaneous locomotion of hygrobots under spatial gradient of humidity. (**A**) Spatial distribution of relative humidity at 23°C near a moist filter paper. Error bars indicate SD. (**B**) Schematics and experimental images of a hygrobot crawling spontaneously on a moist surface. The angle that the leg makes with the substrate, β, determines the friction coefficient (section S3). (**C**) Temporal evolution of the position of the hygrobot. Velocity of hygrobots powered by the spatial gradient of humidity as a function of (**D**) the active layer thickness and (**E**) the actuator length. Circles and lines correspond to the results of experiment and theory, respectively. Inset of (E) shows the overlapped images of hygrobots of different lengths.

at the closest and farthest positions of the hygrobot from the moist surface. Thus, it depends on the bending curvature of the bilayer and the ratchet deformation. We plot the speed of hygrobots as a function of thickness of the active layer and length in Fig. 4, D and E, respectively.

With the increase of the thickness of a thin active layer, the bending moment and thus the curvature of the bilayer increased, which helped the hygrobot to use the greater humidity variation, resulting in an improved locomotion speed (see Fig. 4D). But when the thickness further increased, the bending was completed before the moisture fully diffuses in the active layer. Then, the unsaturated layer restricted bending, leading to the decrease of locomotion speed for the active layer thickness over about 40 μm. Our theoretical prediction correctly captures this trend. The balance between the bending speed and the diffusion rate allows us to find the optimal active layer thickness. The locomotion speed increases with the actuator length (Fig. 4E), because a longer actuator can make a larger vertical displacement to experience a greater humidity difference. Our theory shows a good match with the experimental results.

The ability of the hygrobot to propel itself on a moist surface without an artificial supply of energy opens a wide window of practical applications. In particular, a rich variety of biomedical functions can be performed by the hygrobot on moist human skin (*32*). Small animals, like maggots and leeches, that are capable of autonomous locomotion have already been used on unhealthy skins and tissues for medical therapy over a long period of time (*33*, *34*). In these applications, microrobots have a great potential to replace the living creatures. We have tested the capability of the hygrobot to inhibit bacteria growth from a model skin without any artificial energy supply for locomotion. A hygrobot with antibiotics [cephalosporin (0.8 g/liter) in 67 weight % (wt %) aqueous glycerine] coated on its legs was placed on an agar plate (Fig. 5A), an enriched medium to cultivate bacteria. The bacteria (*Staphylococcus aureus*) were inoculated over the entire agar surface. Because of the humidity gradient in the air above the moist agar plate, the hygrobot moved spontaneously to traverse the 9-cm-diameter petri dish in 10 min, leaving a trail of antibiotics that was dyed blue (Fig. 5B). Then, the plate was incubated at 37°C at humidity above 95% and CO_2 concentration of 5% for 24 hours. A sterilized lane formed in the middle, whose width broadened compared with the initial trail of antibiotics due to diffusion, whereas the rest of the area was cultured to confluency (Fig. 5C).

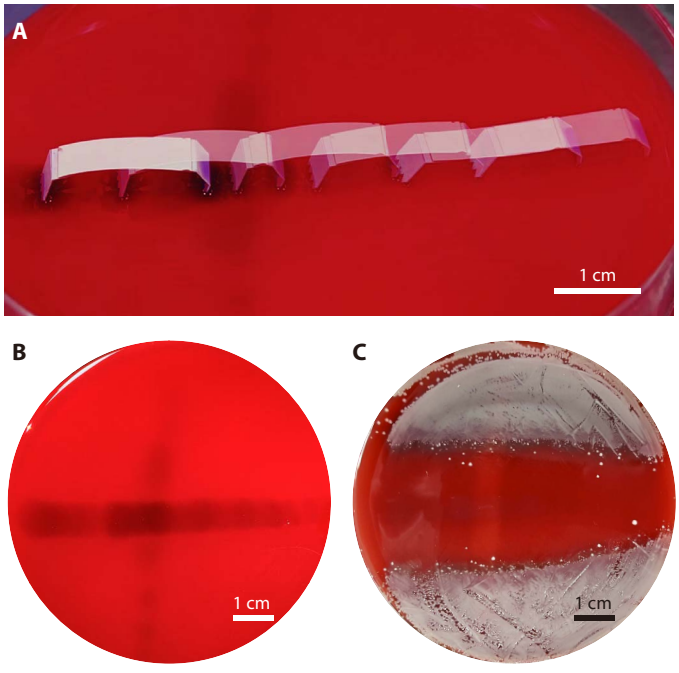

Fig. 5. Power-free sterilization of culture plate. (**A**) Overlapped images of the hygrobot, with its legs coated with antibiotics, crawling on the agar plate as powered by spatial humidity gradient. (**B**) Horizontal trail of the antibiotics applied by the hygrobot. (**C**) Sterilized region after 24-hour incubation coincides with the hygrobot trail.

DISCUSSION

Inspired by the motile awns of some plant seeds with aligned fibrous structure of hygroscopically responsive layer, we have fabricated a bilayer actuator that can bend with great speed and magnitude in response to change in environmental humidity. The oscillatory motion of the actuator with periodic change of humidity has been rectified into directional locomotion by attaching legs with asymmetric friction coefficients. In addition to temporal change of humidity, the spatial gradient of humidity that exists naturally above moist surfaces has been shown to power the hygrobot without requiring any human intervention. We have theoretically modeled the moisture diffusion and consequent swelling and bending of the actuator, which allowed us to predict the speed of the hygrobot and to optimize the actuator design for maximum locomotion speed.

The ability of the hygrobot to propel itself without any artificial energy can be exploited in a variety of applications. Just as with motile seeds, it can actuate military and environmental robots deployed on the ground in response to temporal changes in environmental humidity. On intrinsically moist biological materials, including human skin, it can perform various biomedical treatments while crawling as powered by spatial humidity gradient. By using materials that respond to gases other than water vapor, we may be able to build sensors that produce mechanical responses to the concentration of specific gas molecules.

For practical applications, the enhanced speed and magnitude of the mechanical response to humidity change would play a critical role. On the basis of our finding that the directionally deposited nanofibers lead to agile and large-magnitude responses, further development of fabrication processes to print finer nanofibers with sufficient strength is called for. Although we have focused on pure bending actuators to enable linear locomotion by exploiting the spatial humidity gradient formed normal to the moist surface, different modes of mechanical actuation are possible by controlling the fiber alignment angle with respect to the major axis of slender actuators. The simultaneous generation of twisting and bending can lead to various locomotion modes, including rotation, screwing, and tumbling. The actuation system fabricated and mathematically analyzed here serves as a model that senses, responds to, and interacts with microscale environmental conditions while harvesting energy from nature, just as its biological counterparts, motile plant seeds.

MATERIALS AND METHODS

We used PEO as the hygroscopically active material for its superior hygroexpansivity and biocompatibility. To arrange PEO in thin fibers, we used the electrospinning process, where the 10 wt % aqueous PEO solution was ejected in nanojets from the tip of metal capillary

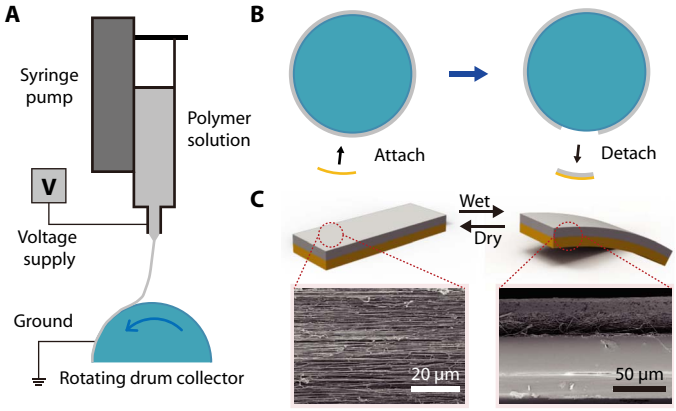

Fig. 6. Fabrication of bilayer actuator composed of a hygroscopically active layer with aligned nanofibers and an inactive layer. (**A**) Experimental apparatus to directionally electrospin nanofibers of polymer solution. (**B**) Formation of bilayer structure by detaching the active layer from the collector drum with the adhesive inactive layer. (**C**) Schematic of the bending deformation of the bilayer and SEM images. Left: Top view of the active layer. Right: Cross-section of the bilayer.

under a strong electrical field, 1.12 kV/mm (*35*). To circumvent chaotic piling of the electrified nanojets because of the coulombic repulsion, we collected the nanojets on the surface of a metal drum that rotates at the same linear speed as the jet, 3.5 m/s, a process called directional electrospinning (Fig. 6A). The thickness of the deposited layer varies from 1 to 100 μm depending on the jetting duration. The solidified PEO fibers that were aligned along the direction of the drum rotation were detached from the collector surface using a sticky polyimide (PI) tape (Fig. 6B). Because PI is hygroscopically inactive, the bilayer structure consisting of an aligned hygroexpansive fiber layer and an inactive layer was completed. The inactive layer consists of 30-μm-thick PI and 25-μm-thick silicone adhesive of different elastic moduli, which were accounted for in our mechanical model. The fabrication details are given in section S1. Figure 6C shows the scanning electron microscopy (SEM) images of the bilayer, where PEO fibers (350 ± 25 nm in average diameter) are arranged in a single direction.

SUPPLEMENTARY MATERIALS

robotics.sciencemag.org/cgi/content/full/3/14/eaar2629/DC1
Section S1. Experimental details of the electrospinning process
Section S2. Various designs of hygrobot
Section S3. Asymmetric friction coefficients of the ratchets
Section S4. Ratchet design to harness spatial gradient of humidity
Section S5. Data of locomotion speed and mass of animals and robots
Fig. S1. Static friction coefficients of ratchets.
Table S1. Locomotion speed and mass data of mammals.
Table S2. Locomotion speed and mass data of non-mammals.
Table S3. Locomotion speed and mass data of walking robots.
Movie S1. Locomotion of a hygrobot under temporal variation of environmental humidity.
Movie S2. Locomotion of various designs of hygrobot.
References (*36*–*77*)

REFERENCES AND NOTES

1. C. Dawson, J. F. V. Vincent, A.-M. Rocca, How pine cones open. *Nature* **390**, 668 (1997).
2. R. Elbaum, L. Zaltzman, I. Burgert, P. Fratzl, The role of wheat awns in the seed dispersal unit. *Science* **316**, 884–886 (2007).
3. D. Evangelista, S. Hotton, J. Dumais, The mechanics of explosive dispersal and self-burial in the seeds of the filaree, *Erodium cicutarium* (Geraniaceae). *J. Exp. Biol.* **214**, 521–529 (2011).
4. W. Jung, W. Kim, H.-Y. Kim, Self-burial mechanics of hygroscopically responsive awns. *Integr. Comp. Biol.* **54**, 1034–1042 (2014).
5. E. Katifori, S. Alben, E. Cerda, D. R. Nelson, J. Dumais, Foldable structures and the natural design of pollen grains. *Proc. Natl. Acad. Sci. U.S.A.* **107**, 7635–7639 (2010).
6. S. Armon, E. Efrati, R. Kupferman, E. Sharon, Geometry and mechanics in the opening of chiral seed pods. *Science* **333**, 1726–1730 (2011).
7. M. J. Harrington, K. Razghandi, F. Ditsch, L. Guiducci, M. Rueggeberg, J. W. C. Dunlop, P. Fratzl, C. Neinhuis, I. Burgert, Origami-like unfolding of hydro-actuated ice plant seed capsules. *Nat. Commun.* **2**, 337 (2011).
8. R. Yoshida, K. Uchida, Y. Kaneko, K. Sakai, A. Kikuchi, Y. Sakurai, T. Okano, Comb-type grafted hydrogels with rapid de-swelling response to temperature changes. *Nature* **374**, 240–242 (1995).
9. V. Magdanz, G. Stoychev, L. Ionov, S. Sanchez, O. G. Schmidt, Stimuli-responsive microjets with reconfigurable shape. *Angew. Chem. Int. Ed.* **53**, 2673–2677 (2014).
10. M. Ji, N. Jiang, J. Chang, J. Sun, Near-infrared light-driven, highly efficient bilayer actuators based on polydopamine-modified reduced graphene oxide. *Adv. Funct. Mater.* **24**, 5412–5419 (2014).
11. L. T. de Haan, A. P. H. J. Schenning, D. J. Broer, Programmed morphing of liquid crystal networks. *Polymer* **55**, 5885–5896 (2014).
12. E. Wang, M. S. Desai, S.-W. Lee, Light-controlled graphene-elastin composite hydrogel actuators. *Nano Lett.* **13**, 2826–2830 (2013).
13. Z. Hu, X. Zhang, Y. Li, Synthesis and application of modulated polymer gels. *Science* **269**, 525–527 (1995).
14. P. Techawaitchai, M. Ebara, N. Idota, T.-A. Asho, A. Kikuchi, T. Aoyagi, Photo-switchable control of pH-responsive actuators via pH jump reaction. *Soft Matter* **8**, 2844–2851 (2012).
15. Q. Zhao, J. W. C. Dunlop, X. Qiu, F. Huang, Z. Zhang, J. Heyda, J. Dzubiella, M. Antonietti, J. Yuan, An instant multi-responsive porous polymer actuator driven by solvent molecule sorption. *Nat. Commun.* **5**, 4293 (2014).
16. P. Chen, Y. Xu, S. He, X. Sun, S. Pan, J. Deng, D. Chen, H. Peng, Hierarchically arranged helical fibre actuators driven by solvents and vapours. *Nat. Nanotechnol.* **10**, 1077–1083 (2015).
17. L. D. Zarzar, P. Kim, J. Aizenberg, Bio-inspired design of submerged hydrogel-actuated polymer microstructures operating in response to pH. *Adv. Mater.* **23**, 1442–1446 (2011).
18. E. Reyssat, L. Mahadevan, How wet paper curls. *Europhys. Lett.* **93**, 54001 (2011).
19. M. Lee, S. Kim, H.-Y. Kim, L. Mahadevan, Bending and buckling of wet paper. *Phys. Fluids* **28**, 042101 (2016).
20. J. Y. Chung, H. King, L. Mahadevan, Evaporative microclimate driven hygrometers and hygromotors. *Europhys. Lett.* **107**, 64002 (2014).
21. M. Mao, L. Guo, D. G. Anderson, R. Langer, Bio-inspired polymer composite actuator and generator driven by water gradients. *Science* **339**, 186–189 (2013).
22. X. Chen, L. Mahadevan, A. Driks, O. Sahin, *Bacillus* spores as building blocks for stimuli-responsive materials and nanogenerators. *Nat. Nanotechnol.* **9**, 137–141 (2014).
23. X. Chen, D. Goodnight, Z. Gao, A. H. Cavusoglu, N. Sabharwal, M. DeLay, A. Driks, O. Sahin, Scaling up nanoscale water-driven energy conversion into evaporation-driven engines and generators. *Nat. Commun.* **6**, 7346 (2015).
24. Y. Abraham, C. Tamburu, E. Klein, J. W. C. Dunlop, P. Fratzl, U. Raviv, R. Elbaum, Tilted cellulose arrangement as a novel mechanism for hygroscopic coiling in the stork's bill awn. *J. R. Soc. Interface* **9**, 640–647 (2012)
25. A. Rafsanjani, V. Brulé, T. L. Western, D. Pasini, Hydro-responsive curling of the resurrection plant *Selaginella lepidophylla*. *Sci. Rep.* **5**, 8064 (2015).
26. J. Yoon, S. Cai, Z. Suo, R. C. Hayward, Poroelastic swelling kinetics of thin hydrogel layers: Comparison of theory and experiment. *Soft Matter* **6**, 6004–6012 (2010).
27. J. C. M. Garnett, Optical properties of thin solid films. *Philos. Trans. R. Soc. London* **203**, 385 (1904).
28. E. L. Cussler, *Diffusion Mass Transfer in Fluid Systems* (Cambridge Univ. Press, 1997).
29. L. Mahadevan, S. Daniel, M. K. Chaudhury, Biomimetic ratcheting motion of a soft, slender, sessile gel. *Proc. Natl. Acad. Sci. U.S.A.* **101**, 23–26 (2004).
30. S. Kim, M. Spenko, S. Trujillo, B. Heyneman, V. Mattoli, M. R. Cutkosky, Whole body adhesion: Hierarchical, directional and distributed control of adhesive forces for a climbing robot, *Proceedings of the IEEE International Conference on Robotics and Automation*, Roma, Italy, 10 to 14 April 2007 (IEEE, 2007).
31. S. Mezoff, N. Papastathis, A. Takesian, B. A. Trimmer, The biomechanical and neural control of hydrostatic limb movements in *Manduca sexta*. *J. Exp. Biol.* **207**, 3043–3053 (2004).
32. G. E. Burch, T. Winsor, Rate of insensible perspiration(diffusion of water) locally through living through dead human skin. *Arch. Intern. Med.* **74**, 437–444 (1944).
33. R. A. Sherman, Maggot therapy for treating diabetic foot ulcers unresponsive to conventional therapy. *Diabetes Care* **26**, 446–451 (2003).
34. C. L. Haycox, P. B. Odland, M. D. Coltrera, G. J. Raugi, Indications and complications of medicinal leech therapy. *J. Am. Acad. Dermatol.* **33**, 1053–1055 (1995).
35. J. M. Deitzel, J. Kelinmeyer, D. Harris, N. C. B. Tan, The effect of processing variables on the morphology of electrospun nanofibers and textiles. *Polymer* **42**, 261–272 (2001).
36. J. Iriarte-Díaz, Differential scaling of locomotor performance in small and large terrestrial mammals. *J. Exp. Biol.* **205**, 2897–2908 (2002).

37. T. Garland Jr., The relation between maximal running speed and body mass in terrestrial mammals. *J. Zool.* **199**, 157–170 (1983).
38. M. Djawdan, T. Garland Jr., Maximal running speeds of bipedal and quadrupedal rodents. *J. Mammal.* **69**, 765–772 (1988).
39. T. Garland Jr., F. Geiser, R. V. Baudinette, Comparative locomotor performance of marsupial and placental mammals. *J. Zool.* **215**, 505–522 (1988).
40. T. Garland Jr., C. M. Janis, Does metatarsal/femur ratio predict maximal running speed in cursorial mammals? *J. Zool.* **229**, 133–151 (1993).
41. M. Silva, Allometric scaling of body length: Elastic or geometric similarity in mammalian design. *J. Mammal.* **79**, 20–32 (1998).
42. R. M. Nowak, *Walker's Mammals of the World* (Johns Hopkins Univ. Press, 1999).
43. G. A. Bartholomew, J. R. B. Lighton, G. N. Louw, Energetics of locomotion and patterns of respiration in tenebrionid beetles from the Namib Desert. *J. Comp. Physiol. B* **155**, 155–162 (1985).
44. G. C. Wu, J. C. Wright, D. L. Whitaker, A. N. Ahn, Kinematic evidence for superfast locomotory muscle in two species of teneriffiid mites. *J. Exp. Biol.* **213**, 2551–2556 (2010).
45. R. McN. Alexander, G. M. O. Maloiy, R. Njau, A. S. Jayes, Mechanics of running of the ostrich (*Struthio camelus*). *J. Zool.* **187**, 169–178 (1979).
46. R. J. Full, M. S. Tu, Mechanics of a rapid running insect: Two-, four- and six-legged locomotion. *J. Exp. Biol.* **156**, 215–231 (1991).
47. F. D. Duncan, R. M. Crewe, A comparison of the energetics of foraging of three species of *Leptogenys* (Hymenoptera, Formicidae). *Physiol. Entomol.* **18**, 372–378 (1993).
48. S. Maeda, Y. Hara, T. Sakai, R. Yoshida, S. Hashimoto, Self-walking gel. *Adv. Mater.* **19**, 3480–3484 (2007).
49. N. Cheng, G. Ishigami, S. Hawthorne, H. Chen, M. Hansen, M. Telleria, R. Playter, K. Iagnemma, Design and analysis of a soft mobile robot composed of multiple thermally activated joints driven by a single actuator, *Proceedings of the 2010 IEEE International Conference on Robotics and Automation*, Anchorage, AK, 3 to 8 May 2010 (IEEE, 2010).
50. W. Wang, J.-Y. Lee, H. Rodrigue, S.-H. Song, W.-S. Chu, S.-H. Ahn, Locomotion of inchworm-inspired robot made of smart soft composite (SSC). *Bioinspir. Biomim.* **9**, 046006 (2014).
51. C. D. Onal, D. Rus, Autonomous undulatory serpentine locomotion utilizing body dynamics of a fluidic soft robot. *Bioinspir. Biomim.* **8**, 026003 (2013).
52. K. Jung, J. C. Koo, J.-d. Nam, Y. K. Lee, H. R. Choi, Artificial annelid robot driven by soft actuators. *Bioinspir. Biomim.* **2**, S42–S49 (2007).
53. B. Kim, M. G. Lee. Y. P. Lee, Y. Kim, G. Lee, An earthworm-like micro robot using shape memory alloy actuator. *Sens. Actuators A Phys.* **125**, 429–437 (2006).
54. N. Tomita, K. Takagi, K. Asaka, Development of a quadruped soft robot with fully IPMC body, *Proceedings of SICE Annual Conference 2011*, Tokyo, Japan, 13 to 18 September 2011 (Waseda University, 2011).
55. L. Shi, S. Guo, K. Asaka, S. Mao, Development and experiments of a novel multifunctional underwater microrobot, *Proceedings of the 2010 IEEE International Conference on Nano/Molecular Medicine and Engineering*, Hong Kong, 5 to 9 December 2010 (IEEE, 2010).
56. S. Guo, L. Shi, K. Asaka, IPMC actuator-based an underwater microrobot with 8 legs, *Proceedings of 2008 IEEE International Conference on Mechatronics and Automation*, Chengdu, China, 5 to 8 August 2008 (IEEE, 2008).
57. W. Zhang, S. Guo, K. Asaka, Development of an underwater biomimetic microrobot with compact structure and flexible locomotion. *Microsyst. Technol.* **13**, 883–890 (2007).
58. C. T. Nguyen, H. Phung, H. Jung, U. Kim, T. D. Nguyen, J. Park, H. Moon, J. C. Koo, H. R. Choi, Printable monolithic hexapod robot driven by soft actuator, *Proceedings of the 2015 IEEE International Conference on Robotics and Automation (ICRA)*, Seattle, WA, 26 to 30 May 2015 (IEEE, 2015).
59. S. W. Kwok, S. A. Morin, B. Mosadegh, J.-H. So, R. F. Shepherd, R. V. Martinez, B. Smith, F. C. Simeone, A. A. Stokes, G. M. Whitesides, Magnetic assembly of soft robots with hard components. *Adv. Funct. Mater.* **24**, 2180–2187 (2014).
60. Y. Ma, Y. Zhang, B. Wu, W. Sun, Z. Li, J. Sun, Polyelectrolyte multilayer films for building energetic walking devices. *Angew. Chem.* **123**, 6378–6381 (2011).
61. D. Morales, E. Palleau, M. D. Dickey, O. D. Velev, Electro-actuated hydrogel walkers with dual responsive legs. *Soft Matter* **10**, 1337–1348 (2014).
62. S.-W. Lee, J. H. Prosser, P. K. Purohit, D. Lee, Bioinspired hygromorphic actuator exhibiting controlled locomotion. *ACS Macro Lett.* **2**, 960–965 (2013).
63. M. Raibert, Trotting, pacing and bounding by a quadruped robot. *J. Biomech.* **23**, 79–81 (1990).
64. Y. Fukuoka, H. Kimura, A. H. Cohen, Adaptive dynamic walking of a quadruped robot on irregular terrain based on biological concepts. *Int. J. Robotics Res.* **22**, 187–202 (2003).
65. Y. Fukuoka, H. Kimura, Dynamic locomotion of a biomorphic quadruped 'Tekken' robot using various gaits: Walk, trot, free-gait and bound. *Appl. Bionics Biomech.* **6**, 63–71 (2009).
66. N. Kohl, P. Stone, Policy gradient reinforcement learning for fast quadrupedal locomotion, *Proceedings of the 2004 IEEE International Conference on Robotics and Automation (ICRA)*, New Orleans, LA, 26 April to 1 May 2004 (IEEE, 2004).
67. F. Iida, R. Pfeifer, *Cheap Rapid Locomotion of a Quadruped Robot: Self-Stabilization of Bounding Gait* (Intelligent Autonomous Systems, IOP Press, 2004), vol. 8.
68. I. Poulakakis, J. A. Smith, M. Buehler, Modeling and experiments of untethered quadrupedal running with a bounding gait: The scout II robot. *Int. J. Robotics Res.* **24**, 239–256 (2005).
69. F. Iida, G. Gomez, R. Pfeifer, Exploiting body dynamics for controlling a running quadruped robot, *Proceedings of the 12th International Conference on Advanced Robotics (ICAR)*, Seattle, WA, 18 to 20 July 2005 (IEEE, 2005).
70. H. Kimura, Y. Fukuoka, A. H. Cohen, Adaptive dynamic walking of a quadruped robot on natural ground based on biological concepts. *Int. J. Robotics Res.* **26**, 475–490 (2007).
71. M. Raibert, K. Blankespoor, G. Nelson, R. Playter, BigDog, the rough-terrain quadruped robot. *Proc. IFAC* **41**, 10822–10825 (2008).
72. J. Estremera, K. J. Waldron, Thrust control, stabilization and energetics of a quadruped running robot. *Int. J. Robotics Res.* **27**, 1135–1151 (2008).
73. S. Rutishauser, A. Spröwitz, L. Righetti, A. J. Ijspeert, Passive compliant quadruped robot using central pattern generators for locomotion control, *Proceedings of the 2nd Biennial IEEE/RAS-EMBS International Conference on Biomedical Robotics and Biomechatronics*, Scottsdale, AZ, 19 to 22 October 2008 (2008).
74. Z. G. Zhang, H. Kimura, Rush: A simple and autonomous quadruped running robot. *Proc. IMechE* **223**, 323–336 (2009).
75. J. A. Smith, I. Poulakakis, M. Trentini, I. Sharf, Bounding with active wheels and liftoff angle velocity adjustment. *Int. J. Robotics Res.* **29**, 414–427 (2010).
76. C. Semini, N. G. Tsagarakis, E. Guglielmino, M. Focchi, F. Cannella, D. G. Caldwell, Design of HyQ—A hydraulically and electrically actuated quadruped robot. *Proc. IMechE* **225**, 831–849 (2011).
77. A. Spröwitz, A. Tuleu, M. Vespignani, M. Ajallooeian, E. Badri, A. J. Ijspeert, Towards dynamic trot gait locomotion: Design, control, and experiments with Cheetah-cub, a compliant quadruped robot. *Int. J. Robotics Res.* **32**, 923–950 (2013).

Funding: This work was supported by the Samsung Research Funding and Incubation Center (grant SRFC-MA1301-05), National Research Foundation of Korea (grant 2016901290), and Bio-Mimetic Robot Research Center funded by the Defense Acquisition Program Administration under grant UD130070ID. **Author contributions:** B.S. performed all experiments. B.S., J.H., M.L., K.P., and H.-Y.K. made theoretical models. G.H.P. and T.H.C. performed bacteria sterilization experiment. K.-J.C. and H.-Y.K. designed experiments. B.S. and H.-Y.K. analyzed the data and wrote the paper. H.-Y.K. conceived and supervised the research. **Competing interests:** H.-Y.K., B.S., M.L., and J.H. are inventors on patent application (#10-2017-0086468, Republic of Korea) submitted by SNU R&DB Foundation that covers a fabrication method for a hygroscopically responsive actuator and how to use the actuator to drive a robot capable of linear locomotion. H.-Y.K., B.S., M.L., and J.H. are inventors on patent application (#10-2016-0023692, Republic of Korea) submitted by SNU R&DB Foundation that covers an indicator of relative humidity operating on the basis of hygroexpansive nature of hygroscopic nanofibers. All other authors declare that they have no competing interests. **Data and materials availability:** All data needed to evaluate the study are in the main text or the supplementary materials. For more detailed information on materials and methods, contact H.-Y.K.

Submitted 19 October 2017
Accepted 3 January 2018
Published 24 January 2018
10.1126/scirobotics.aar2629

Citation: B. Shin, J. Ha, M. Lee, K. Park, G. H. Park, T. H. Choi, K.-J. Cho, H.-Y. Kim, Hygrobot: A self-locomotive ratcheted actuator powered by environmental humidity. *Sci. Robot.* **3**, eaar2629 (2018).

Hygrobot: A self-locomotive ratcheted actuator powered by environmental humidity

Beomjune Shin, Jonghyun Ha, Minhee Lee, Keunhwan Park, Gee Ho Park, Tae Hyun Choi, Kyu-Jin Cho and Ho-Young Kim

Sci. Robotics **3**, eaar2629.
DOI: 10.1126/scirobotics.aar2629

Science Robotics

robotics.sciencemag.org/cgi/content/full/3/14/eaar2629/DC1

Supplementary Materials for

Hygrobot: A self-locomotive ratcheted actuator powered by environmental humidity

Beomjune Shin, Jonghyun Ha, Minhee Lee, Keunhwan Park, Gee Ho Park, Tae Hyun Choi, Kyu-Jin Cho, Ho-Young Kim*

*Corresponding author. Email: hyk@snu.ac.kr

Published 24 January 2018, *Sci. Robot.* **3**, eaar2629 (2018)
DOI: 10.1126/scirobotics.aar2629

The PDF file includes:

Other Supplementary Material for this manuscript includes the following:
(available at robotics.sciencemag.org/cgi/content/full/3/14/eaar2629/DC1)

Movie S1 (.mov format). Locomotion of a hygrobot under temporal variation of environmental humidity.
Movie S2 (.mov format). Locomotion of various designs of hygrobot.

Section S1. Experimental details of the electrospinning process

The electrospinning apparatus consists of a syringe pump, a syringe with 25 G stainless steel capillary at its end, and a high voltage supply. The liquid used is 10 wt% aqueous polymer solution of polyethylene oxide (PEO, viscosity-average molecular weight 300,000 g/mol, Sigma Aldrich). The distance between the end of the tip and the drum collector, which is 20 cm in diameter and rotates in 700 rpm, is 10 cm. The voltage applied to the polymer drop is 11.2 kV. All the processes were carried out at 25% RH (relative humidity) and 25°C.

Section S2. Various designs of hygrobot

We show various types of hygrobots that can propel themselves in response to change of environmental humidity in Fig. 3F. The top row shows the configurations of the hygrobots in the dry state, and the bottom row the wet state. (1) The hygrobot in the first column resembles a broom, whose stick is curled when dry. When wet, the stick is straightened out while the end of the stick acts as a ratchet, so that the brush-like part advances. As it is dried, the front brush is fixed while the stick advances with curling. (2) The second column shows a hygrobot that bends in a similar fashion to the hygrobot analyzed in the main text as shown in Fig. 2C. But here the ratchets are made of PDMS (polydimethylsiloxane) whose surfaces are incised in a tilted direction (Ref. *29* in main text) to achieve axisymmetric friction. (3) The third column resembles a snake, standing vertically on the side edges of the bilayer. Under a high relative humidity, it is straightened out while the rear end is fixed thanks to the ratchet. When it is curled under a dry condition, the front end is fixed. (4) The fourth hygrobot employs a bilayer actuator standing on its side which changes its sense of curvature depending on the humidity. It has two feet on its ends and a long and slender neck sticking out to the front. As the humidity increases, the bilayer bends to push the neck forward with the feet fixed. The bilayer bends in the other direction when dried, to move its feet forward while the neck is fixed.

Section S3. Asymmetric friction coefficients of the ratchets

We measured the static friction coefficients, μ, of the ratchets employed in our hygrobot. As shown in Fig. S1A, an object sitting on a filter paper starts to move when the inclination exceeds a critical value, θ. The balance between friction and gravity leads to $\mu = \tan\theta$.

Fig. S1B displays the static friction coefficients of the ratchets adopted for locomotion under temporal humidity variation. When the environmental humidity increases, the bilayer bends upward to make the two legs come closer. The friction coefficient of the hind leg (on its knee) is lower than that of the foreleg (on its tip), so that only the hind leg advances. As the atmosphere becomes dry, the bilayer bends downward pushing the two legs apart. In this case, only the foreleg (on its knee) having a lower friction coefficient moves forward while the hind leg (on its tip) is fixed.

Fig. S1C shows the static friction coefficients of the ratchets of the hygrobot that propels itself under spatial humidity gradient. We use the dependence of the friction coefficient on the angle β that the leg makes with the substrate – μ increases with β. The hind leg has a lower β when the legs are pulled closer, while the foreleg has a lower β when the legs are pushed apart.

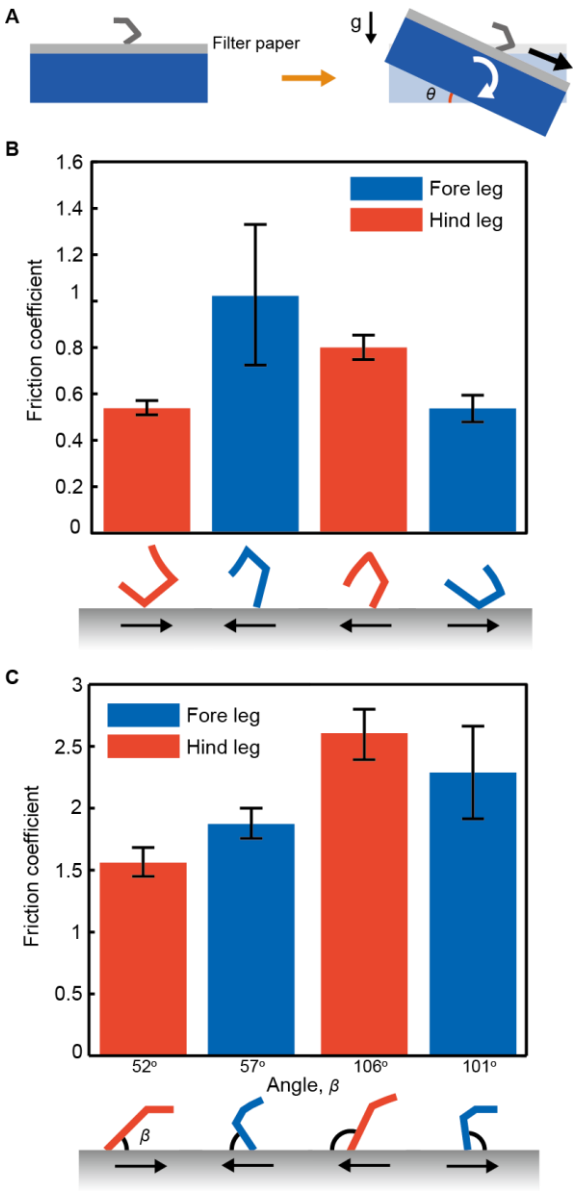

Fig. S1. Static friction coefficients of ratchets. (A) Experimental schematic to measure the static friction coefficient. Static friction coefficients of the fore and hind legs when the actuator curvature reverses its sense for a hygrobot driven by **(B)** temporal variation of humidity and **(C)** spatial gradient of humidity. The arrows in **(B)** and **(C)** indicate the directions of the force acting on the legs by the actuator.

Section S4. Ratchet design to harness spatial gradient of humidity

The ratchet system used for a hygrobot driven by temporal variation of humidity has been designed considering the large degree of bending of the bilayer in both upward and downward directions. The bending causes the dramatic conformational change of the legs so that they either stand on their knees or tips. When the hygrobot is operated in spatial gradient of humidity, the available humidity difference is not as great as in the case of temporal variation, in general. In addition, the hygrobot should be able to move its bilayer actuator vertically to harness the difference of humidity that decreases in a vertical direction. The bilayer located relatively near

the moist surface experiences the swelling of its active layer. Then it should be elevated vertically as well as bend upward (to the inactive layer) to be dried at a region of low humidity. At an elevated location, the bilayer is dried and bends downward (to the active layer) to descend to the region of high humidity.

To facilitate the up-down movement of the bilayer and effectively rectify the relatively small degree of bending, a ratchet system has been developed which changes the friction coefficient sensitively to the variation of the leg's posture without too much deformation. We used the fact that the leg's friction coefficient is a function of the angle, β, that it makes with the substrate as shown in Fig. S1C. The legs having different contact angles β in the front and rear ends of the bilayer successfully rectify the bending oscillation and enable the forward propulsion of the hygrobot on a moist surface.

Section S5. Data of locomotion speed and mass of animals and robots

We provide the data of locomotion speed and mass of animals and robots used to plot Fig. 3E in Tables S1-3.

Table S1. Locomotion speed and mass data of mammals. The table is reproduced from (*36*) with permission.

Species	Body mass (kg)	Maximum speed (BL/s)	Ref.
Proboscidae			
Loxodonta africana	6000	1.4	(*37*, *42*)
Elephas maximus	4000	1.18	(*38*)
Perissodactyla			
Ceratotherium simum	2000	1.79	(*40*, *42*)
Diceros bicornis	1200	3.6	(*40*, *42*)
Equus caballus	350	7.56	(*40*, *42*)
Equus zebra	300	7.35	(*37*, *42*)
Tapirus bairdii	250	5.18	(*40*, *41*)
Equus burchelli	235	8.16	(*40*, *42*)
Equus hemionus	200	8.4	(*40*, *42*)
Artiodactyla			
Hippopotamus amphibius	3800	1.7	(*37*, *42*)
Giraffa cameolopardalis	1075	3.8	(*40*, *42*)
Bison bison	865	5.4	(*40*, *42*)
Bos sauveli	800	3.62	(*37*, *42*)
Syncerus caffer	620	5.6	(*40*, *42*)

Camelus dromedarius	550	3.03	(*40*, *42*)
Taurotragus oryx	511	7.2	(*40*, *42*)
Alces alces	384	5.47	(*40*, *42*)
Cervus elaphus	300	9.04	(*37*, *42*)
Connochaetes gnu	300	10.97	(*37*, *41*)
Hippotragus equinus	226.5	6.65	(*40*, *42*)
Connochaetes taurinis	216	10.88	(*40*, *41*)
Alcelaphus buselaphus	136	10.94	(*40*, *42*)
Damaliscus lunatus	130	11.63	(*40*, *42*)
Oreamnos americanus	113.5	6.36	(*40*, *42*)
Rangifer tarandus	100	12.71	(*40*, *42*)
Lama guanacoe	95	8.77	(*40*, *42*)
Ovis canadensis nelsoni	85	8.96	(*41*)
Phacochoerus aethiopicus	85	12.38	(*37*, *42*)
Odocoileus hemionus	74	11.87	(*40*, *41*)
Capra caucasia	70	7.71	(*37*, *42*)
Ovis ammon	65	10.8	(*37*, *42*)
Gazella granti	62.5	16.67	(*40*, *41*)
Odocoileus virginianus	57	13.59	(*40*, *41*)
Dama dama	55	11.51	(*40*, *42*)
Aepyceros melampus	53.25	9.76	(*40*, *42*)
Antilocapra americana	50	21.6	(*37*, *40*)
Capreolus capreolus	50	13.17	(*37*, *42*)
Rupicapra rupicapra	50	9.82	(*37*, *42*)
Antilope cervicapra	37.5	23.63	(*40*, *42*)
Saiga tatarica	35	18	(*40*, *42*)
Antidorcas marsupialis	34	20.15	(*37*, *42*)
Gazella subgutturosa	30	25.51	(*37*, *41*)
Procapra gutturosa	30	17.78	(*37*, *42*)
Capra aegagrus	30	8.68	(*37*, *42*)
Gazella thomsonii	20.5	24.19	(*40*, *41*)
Madoqua kirki	5	18.29	(*40*, *42*)
Carnivora			

Ursus maritimus	265	4.6	(*42*)
Ursus arctos	251.3	5.76	(*40*, *42*)
Panthera tigris	161	7.2	(*40*, *42*)
Panthera leo	155.8	8.17	(*40*, *42*)
Ursus americanus	93.4	7.85	(*40*)
Acinonyx jubatus	58.8	22.67	(*40*, *42*)
Panthera pardus	52.4	11.49	(*40*, *42*)
Crocuta crocuta	52	13.46	(*40*, *42*)
Canis lupus	35.3	14.13	(*40*, *42*)
Hyaena hyaena	26.8	12.13	(*40*, *42*)
Canis familiaris	25	18.73	(*37*, *41*)
Lycaon pictus	20	20.11	(*37*, *42*)
Canis latrans	13.3	20.06	(*40*, *42*)
Meles meles	11.6	11.01	(*40*, *42*)
Canis aureus	8.8	18.22	(*40*, *42*)
Procyon lotor	7	12.77	(*40*, *42*)
Canis mesomelas o adustus	7	25.66	(*37*, *41*)
Vulpes fulva	4.8	28.69	(*40*, *42*)
Nasua narica	4.4	13.5	(*40*, *42*)
Urocyon cinereoargenteus	3.7	29.59	(*40*, *42*)
Mephitis mephitis	2.5	13.09	(*40*, *42*)
Primates			
Gorilla gorilla	127	5.2	(*37*, *41*)
Homo sapiens	70	7.93	(*37*, *42*)
Presbytis	13	19.4	(*37*, *42*)
Rodentia			
Marmota monax	4	9.6	(*37*, *42*)
Uromys caudimaculatus	1.18	16.63	(*39*, *42*)
Sciurus niger	1.078	19.17	(*39*, *41*)
Spermophilopsis leptodactylus	0.6	34.98	(*37*, *41*)
Spermophilus undulatus	0.6	19.43	(*37*, *41*)
Spermophilus citellus	0.5	18.59	(*37*, *41*)
Sciurus carolinensis	0.5	30.98	(*39*, *41*)

Sciurus vulgaris and persicus	0.4	22.25	(*37*, *41*)
Spermophilus beldingi	0.3	15.92	(*37*, *41*)
Rattus	0.25	13.78	(*37*, *42*)
Spermophilus saturatus	0.222	30.06	(*39*, *41*)
Tamiasciurus hudsonicus	0.22	20.51	(*37*, *42*)
Spermophilus tridecemlineatus	0.125	20.02	(*39*, *41*)
Spermophilus tereticaudus	0.1126	25.82	(*38*, *41*)
Neotoma lepida	0.1106	24.3	(*38*, *42*)
Mesocricetus brandti	0.11	13.89	(*37*, *42*)
Tamias striatus	0.1	14.21	(*37*, *42*)
Dipodomys deserti	0.0976	26.73	(*38*, *41*)
Ammospermophilus leucurus	0.0759	30.45	(*38*, *42*)
Pseudomys nanus	0.061	30.02	(*39*, *41*)
Zymomys argurus	0.0605	25.56	(*39*, *42*)
Dipodomys microps	0.056	45.05	(*37*, *41*)
Tamias amoenus	0.051	42.94	(*39*)
Microtus pennsylvanicus	0.05	24.51	(*37*, *41*)
Pseudomys australis	0.05	36.54	(*39*, *41*)
Heteromys dasmarestianus	0.05	22.88	(*39*, *42*)
Dipodomys ordii	0.0478	31.89	(*38*, *41*)
Lyomis pictus	0.042	40.03	(*39*, *42*)
Chaetodipus baileyi	0.0391	29.99	(*38*, *41*)
Dipodomys merriami	0.035	80.31	(*37*, *41*)
Notomys cervinus	0.035	35.14	(*39*, *41*)
Pitymys pinetorum	0.03	17.97	(*37*, *41*)
Tamias minimus	0.0293	44.74	(*38*, *41*)
Zapus trinotatus	0.0285	38.44	(*39*, *41*)
Peromyscus leucopus	0.025	30.89	(*37*, *41*)
Napeozapus insignis	0.025	25.8	(*37*, *42*)
Notomys alexis	0.0245	37.04	(*37*, *41*)
Perognathus parvus	0.0244	35.39	(*38*, *41*)
Peromyscus eremicus	0.0198	39.77	(*38*, *41*)
Peromyscus truei	0.0193	43.78	(*38*, *41*)

Onychomys torridus	0.0193	24.29	(*38*)
Peromyscus maniculatus	0.0182	41.84	(*38*, *41*)
Chaetodipus fallax	0.018	40.12	(*38*, *41*)
Zapus hudsonicus	0.018	27.89	(*37*, *41*)
Pseudomys hermannbergensis	0.018	39.49	(*39*, *41*)
Mus musculus	0.016	43.88	(*37*, *42*)
Leggadina forresti	0.0155	41.51	(*39*, *42*)
Peromyscus crinitus	0.0137	39.14	(*38*, *41*)
Microdipodops megacephalus	0.0123	38.79	(*38*, *42*)
Perognathus longimembris	0.0089	39.26	(*38*, *41*)
Lagomorpha			
Lepus arcticus	4.6	31.49	(*37*, *41*)
Lepus alleni	4.4	35.96	(*37*, *41*)
Lepus europeus	4	37.12	(*37*)
Lepus townsendii	3.5	30.19	(*37*, *41*)
Lepus californicus	2	41.59	(*37*)
Oryctolagus cuniculus	1.9	37.8	(*37*, *42*)
Lepus americanus	1.5	35.77	(*37*)
Sylvilalagus	1.5	31.49	(*37*, *42*)
Marsupialia			
Macropus spp	50	14.42	(*39*, *41*)
Macropus eugenii	4	22.64	(*39*)
Bettongia penicilata	1.1	18.35	(*39*, *42*)
Potorus tridactylus	0.998	17.56	(*39*, *42*)
Isoodon obesulus	0.718	12.07	(*39*, *42*)
Dasyuroides byrnei	0.12	31.68	(*39*, *42*)
Monodelphis brevicaudata	0.0745	19.86	(*39*, *42*)
Antechinus flavipes	0.052	29.03	(*40*)
Antechinus stuardii	0.0315	39.26	(*39*, *41*)
Antechinomys laniger	0.025	38.76	(*39*, *41*)
Sminthopsis macroura	0.02	40.54	(*39*, *41*)
Sminthopsis crassicaudata	0.017	34.82	(*39*, *41*)
Cercatetus concinnus	0.015	15.92	(*39*, *42*)

Myrmecobius fasciatus	0.48	39.6	(*39*, *42*)

Table S2. Locomotion speed and mass data of non-mammals.

Species	Body mass (kg)	Maximum speed (BL/s)	Ref.
Onymacris plana	0.00073	50	(*43*)
Dolomedes plantarius	0.0015	37.5	(*43*)
Eremobates marathoni	0.002	10	(*43*)
Parateneriffia	0.0000001	100	(*44*)
Struthio camelus	100	68	(*45*)
Periplaneta americana	0.00083	50	(*46*)
Leptogenys schwabi	0.00000896	1.36	(*47*)
Leptogenys nitida	0.00000171	5.82	(*47*)

Table S3. Locomotion speed and mass data of walking robots.

Category	Body mass (g)	Maximum speed (BL/s)	Ref.
Soft robot	0.0012	0.00118	(*48*)
Soft robot	60	0.02632	(*49*)
Soft robot	63	0.0184	(*50*)
Soft robot	900	0.07	(*51*)
Soft robot	30	0.022	(*52*)
Soft robot	9	0.005	(*53*)
Soft robot	3.58	0.016	(*54*)
Soft robot	10	0.024	(*55*)
Soft robot	17	0.138	(*56*)
Soft robot	19	0.105	(*57*)
Soft robot	80	0.022	(*58*)
Soft robot	63	0.039	(*59*)
Soft robot	0.036	0.011	(*60*)
Soft robot	0.052	0.003	(*61*)
Soft robot	0.02	0.024	(*62*)
Rigid robot	38000	2.8	(*63*)
Rigid robot	38000	3.7	(*63*)

Rigid robot	3100	2.2	(*64*)
Rigid robot	3100	4.3	(*65*)
Rigid robot	3100	4.8	(*65*)
Rigid robot	1400	1	(*66*)
Rigid robot	1500	2.9	(*67*)
Rigid robot	20865	2.4	(*68*)
Rigid robot	273	3.5	(*69*)
Rigid robot	4300	3.2	(*70*)
Rigid robot	109000	2.8	(*71*)
Rigid robot	109000	1.5	(*71*)
Rigid robot	109000	1.8	(*71*)
Rigid robot	8000	0.6	(*72*)
Rigid robot	8000	0.6	(*72*)
Rigid robot	720	1.1	(*73*)
Rigid robot	720	0.5	(*73*)
Rigid robot	4300	3	(*74*)
Rigid robot	15700	2.4	(*75*)
Rigid robot	70000	2	(*76*)
Rigid robot	1100	6.9	(*77*)